Experiments in Fluids 18 (1995) 288–302 © Springer-Verlag 1995

Visualization of the structure of supersonic turbulent boundary layers

M. W. Smith, A. J. Smits

Abstract A series of flow visualizations has been performed on two flat-plate zero-pressure-gradient supersonic boundary layers. The two different boundary layers had moderate Mach numbers of 2.8 and 2.5 and Re_θ's of 82,000 and 25,000 respectively. A number of new visualization techniques were applied. One was a variation of conventional schlieren employing "selective cut-off" at the knife edge plane. Motion pictures of the flow were generated with this technique. Droplet seeding was also used to mark the flow, and high speed movies were made to show structure evolution. Still pictures were also taken to show details within the large-scale motions. Finally, Rayleigh scattering was used to construct planar images of the flow. Together, these techniques provide detailed information regarding the character and kinematics of the large-scale motions appearing in boundary layers in supersonic flow. Using these data, in concert with existing hot-wire data, some suggestions are made regarding the characteristics of the "average" large-scale motion.

1 Introduction

This paper presents the results of a series of flow visualization experiments designed to reveal the structure of zero pressure gradient turbulent boundary layers at supersonic Mach numbers. Some previous work has been directed specifically at the visualization of supersonic boundary layers. Deckker [1982], for example, employed a sharp-focus schlieren technique and found large-scale density-gradient structures spanning a shock tube boundary layer. Also, a considerable body of boundary layer visualizations has come with work done for other reasons. For instance, Van Dyke [1982], presents excellent shadowgraphs of projectiles which include boundary layers with obvious large-scale structure.

Received: 1 December 1993 / Accepted: 5 October 1994

M. W. Smith[1], A. J. Smits
Mechanical and Aerospace Engineering Department,
Princeton University,
Princeton, NY 08544, USA

[1] Current address: NASA Langley Research Center, MS 197,
Hampton, VA 23681, USA

This work was supported by the Air Force Office of Scientific Research under Grant 89-0120, monitored by Dr. James M. McMichael. Also, the authors wish to thank Prof. R. B. Miles for his contributions to the Rayleigh scattering portion of this project.

This paper describes the development and use of several new techniques for imaging supersonic boundary layer structure. High-speed schlieren movies were made, using a selective cut-off to reveal the evolution of large-scale structures with strong density gradients in specified directions (Sect. 3). In another technique, acetone droplets were used as a flow marker (similar to the use of smoke in a low-speed flow). With the droplet seeding, movies were made using general illumination and stills obtained using planar illumination (Sect. 4). Finally, Rayleigh scattering was used in an attempt to provide high resolution instantaneous density cross-sections of the boundary layer (Sect. 5).

The images obtained using these new methods graphically illustrate the characteristics of the large-scale motions in supersonic boundary layers. Large-scale bulges are seen, sometimes with sub-scale eddies along their edges. Like their subsonic counterparts, the bulges convect at about $0.9U_e$, and are inclined to the wall at about 45°. The current data provide visual confirmation of flow features suggested by previous workers using single-point techniques like hot-wire anemometry. Together, the visualization and hot-wire data can be used to construct a tentative descriptive model of the three-dimensional structure of the large-scale motions in supersonic boundary layers.

2 Flow characteristics

The studies were performed in two flows. In the first flow, the boundary layer formed on the wall of Princeton's 200 mm × 200 mm blowdown supersonic air tunnel. This boundary layer was documented extensively by Spina and Smits [1987], and Spina et al. [1991], and it was used for all the experiments except the Rayleigh scattering experiment. The data were obtained at a point 1.9 m downstream of the nozzle exit. At this location, $\delta = 28$ mm, $Re_\delta = 1.8$ million, $Re_\theta = 81,900$, $U_e = 580$ m/sec, $M_e = 2.82$, where δ is the boundary layer thickness based on 99% of the total pressure (see Fernholz and Finley 1980), θ is the momentum thickness, and the subscript "e" denotes boundary layer edge properties. In the second flow (for the Rayleigh scattering experiment), the boundary layer developed on the wall of a 13 mm × 26 mm blowdown tunnel. At the measurement location in this smaller tunnel, $Re_\theta = 25,000$, $M_e = 2.5$, and $\delta = 4.2$ mm. In both facilities, the boundary layer developed under near-adiabatic, near-zero-pressure-gradient conditions (constant area duct).

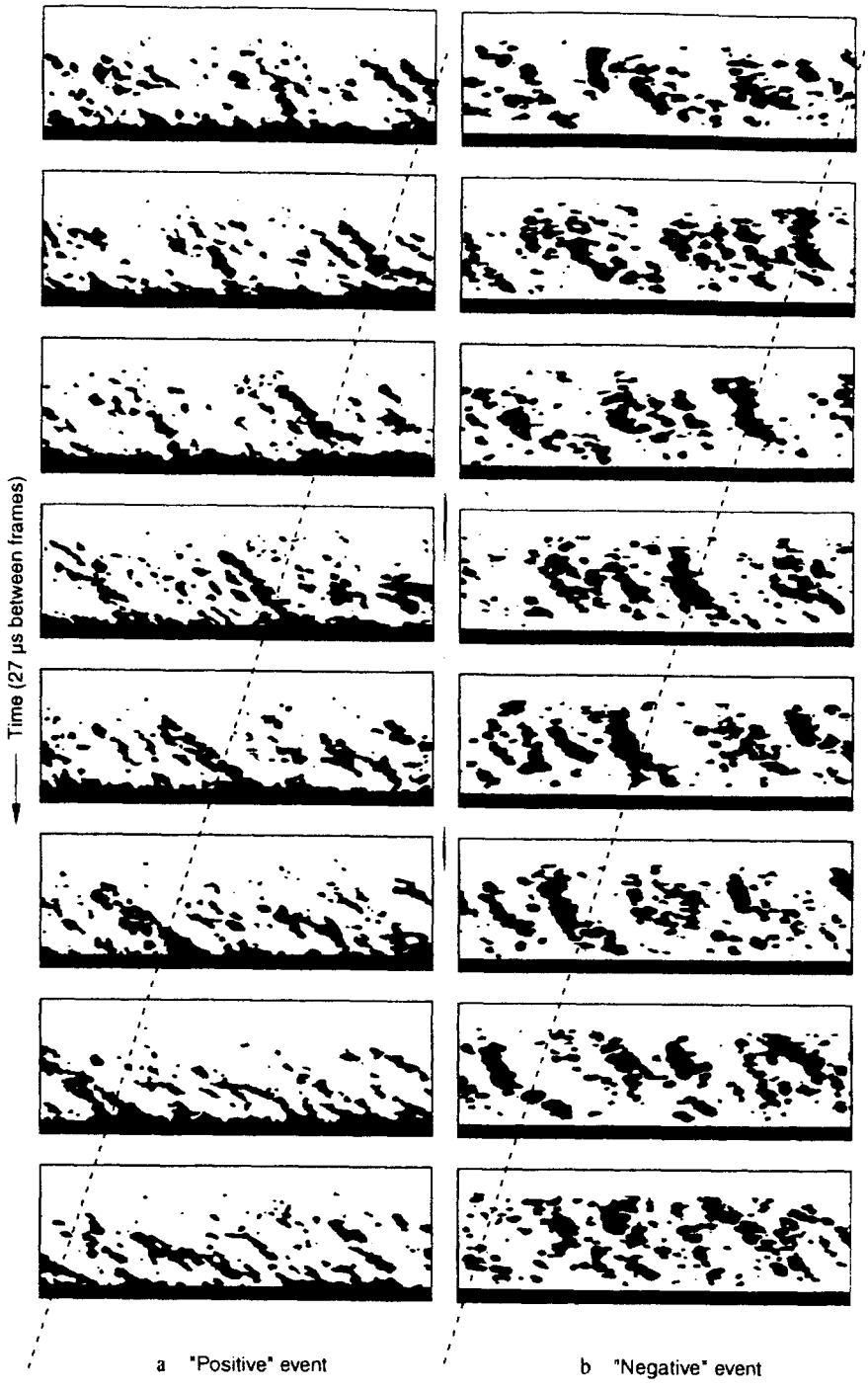

Fig. 1a, b. "Positive" and "negative" density gradient structure sequences acquired with cine schlieren.

3
Cinematographic schlieren

A high-speed movie of schlieren images was made to study the evolution of the large-scale motions in the boundary layer (see M. Smith [1988] for experimental details). Since schlieren is capable of visualizing density gradients in specific directions, the passage of "positive" and "negative" density gradient structures could be examined independently. In this work, "positive" gradient will be used to denote increasing density in the upstream direction. With an acquisition rate of 37,000 frames per second, structures travelling near the freestream velocity were photographed at streamwise intervals of about 0.5δ as they progressed through a streamwise field of view of about 4δ.

Figure 1a is a schlieren sequence exhibiting the passage of strong positive events (dark regions of these images represent positive gradients). A dashed line marks a coherent feature. The passage of a coherent negative event is similarly marked by a dashed line in fig. 1b (in sequence 1b dark regions represent negative gradients). In general, the positive gradient events have a larger magnitude (i.e. the density gradient is stronger). They appear as straight, narrow features attached to the wall and inclined downstream at an angle of between 30° and 50°. The

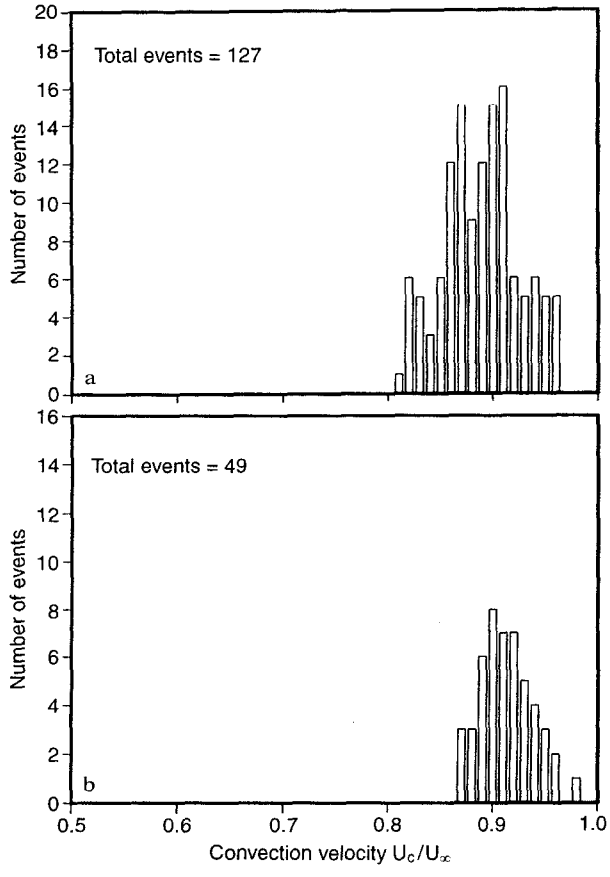

Fig. 2a, b. Distributions of density-gradient structure convection velocities derived from cine schlieren data

negative events are weaker and tend to be steeper, with a less well-defined inclination angle of about 70°.

Careful observation of the first frame of the positive event sequence in Fig. 1a will show that in the vicinity of the dashed line there are two inclined structures, separated in the streamwise direction by a distance of about 0.25δ. As they travel downstream from right to left, the trailing structure appears to catch up to and overtake the leading structure. Although schlieren images contain no information on spanwise position, it might be inferred from this observation that these two structures are of a narrow spanwise extent (relative to the width of the tunnel), that they are separated from each other in the spanwise direction, and that they are travelling at different convection velocities.

Dozens of data records similar to those in Fig. 1 were surveyed and each density-gradient structure was identified visually and its convection velocity was found graphically by using the vertical strip of sequential images as an $x-t$ diagram. The distributions of convection velocities for positive and negative events are given in Fig. 2a and 2b, respectively. The mean value for both distributions is close to $0.9U_e$, with a standard deviation of around $0.1U_e$.

Spina and Smits [1987], and Spina et al. [1991] used hot wires to measure mean convection velocities, distributions of instantaneous convection velocities, and structure angles, all in the same boundary layer used for the current study. They used the "VITA" technique devised by Blackwelder and Kaplan [1976] to locate strong mass-flux gradient "events" in their hot-wire signals.

One can compare the mass-flux data (ρu) generated with hot wires to the schlieren density data (ρ) by considering Morkovin's [1962] Strong Reynolds Analogy (SRA) which states,

$$\frac{\rho'}{\rho} = (\gamma - 1)M^2 \frac{u'}{u} \tag{1}$$

where ρ and ρ' are mean and fluctuating densities, u and u' are mean and fluctuating velocities, and M is the local mean Mach number. D. Smith and Smits [1993] investigated this relation using hot-wire anemometry. Working in the current boundary layer they showed that Eq. (1) is a good approximation, not just for ρ_{rms} and u_{rms} values, but for the instantaneous values ρ' and u' as well. Within this approximation, a high overheat hot-wire signal in this boundary layer may be interpreted as an instantaneous mass-flux time history, or an instantaneous velocity time history, or for the purpose of comparison with schlieren, an instantaneous density time history.

Also, the current visualization data, as well as previous supersonic hot-wire data (e.g. Owen and Horstman [1972]), show that the large-scale structures evolve very little over a streamwise distance many times their typical streamwise length. Thus, Taylor's hypothesis can be applied. Therefore, within the assumptions of Morkovin and Taylor, the hot-wire data (temporal, mass-flux) and the schlieren data (spatial, density) can be compared directly.

In agreement with the schlieren images, Spina and Smits [1987] found that positive mass-flux events are stronger than negative events. Their positive VITA-detected ensemble-averaged mass-flux events display the necessary density gradients required to produce the positive events in the schlieren images (see Fig. 3). The structure angle distributions derived from the positive event schlieren sequence were also in fair

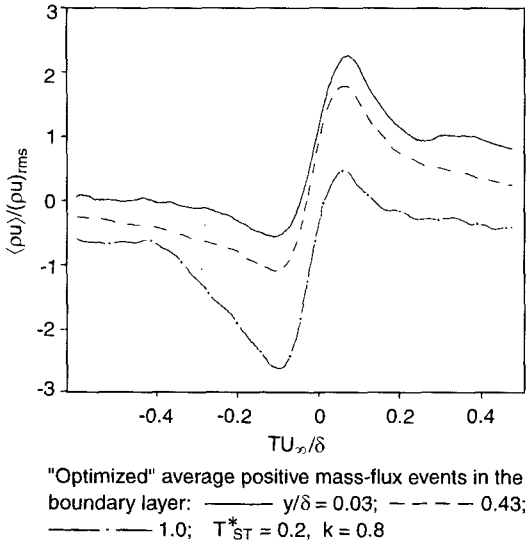

Fig. 3. Ensemble averaged mass-flux events found by Spina et al. using hot wires

agreement with those reported by Spina et al. [1991] (about 50° for the mean). Spina et al. also measured statistics of the instantaneous convection velocity and found a wide distribution of values, as in the present schlieren data. Interestingly, they reported that the convection velocity of the large-scale motions occasionally exceeded the freestream velocity. This may well be due to their measurement technique, since Cogne et al. [1993] found much closer agreement with the present results when using double-pulsed Rayleigh images to determine convection velocities directly from the motion of the large-scale features.

It is possible that the positive and negative density-gradient structures seen in the visualization are really just two different parts of the same structure. The velocity distributions in Fig. 2 show that the positive and negative structures travel at nearly the same mean velocity, about $0.9U_e$. In addition, the ensemble-averaged positive mass-flux hot-wire events near the edge of the boundary layer (Fig. 3, $y/\delta = 1.0$) suggest that a given positive event is composed of a relatively weak negative gradient followed by a stronger positive gradient.

In Fig. 4 a strong negative event and strong positive event have been mated to demonstrate a conjectured structure. This compressible outer-layer turbulent "bulge" is composed of warm, low-density fluid that has moved away from the wall. Its upstream interface is more clearly defined since that positive density gradient boundary is the "leading edge" of the finger as it convects against the freestream at about $0.1U_e$. Also shown in Fig. 4 is the output a mass-flux probe would produce if it were to pass along the dotted line through this density structure. The mass-flux trace dips because the finger is a region of both relatively low density and relatively low velocity. The velocity fluctuations associated with the internal structure of the finger are ignored in this model. This conjectured density trace agrees well with the ensemble-averaged mass-flux event of Fig. 3 (at $y/\delta = 1.0$).

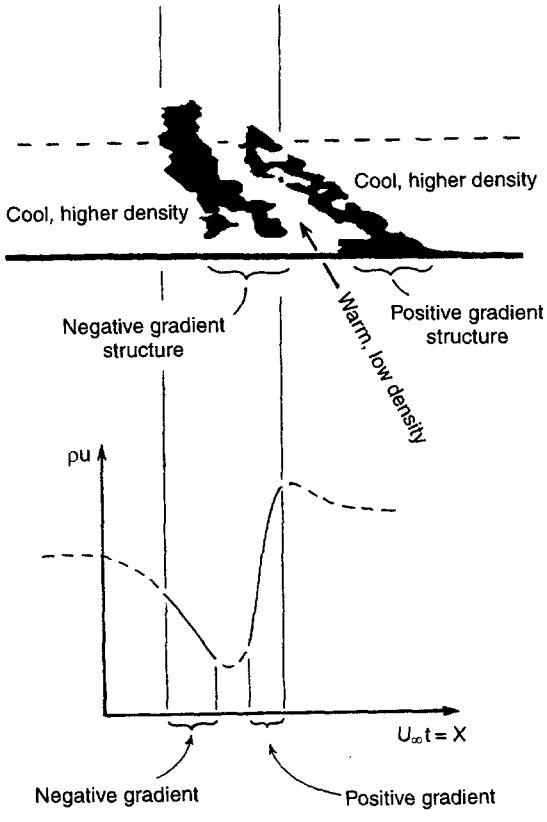

Fig. 4. Suggested relationship of hot-wire mass-flux events and schlieren density gradient events

4
Seeded flow visualizations

Seeded flow visualizations were also performed on the $Re_\theta = 81,900$ $M_e = 2.82$ boundary layer using Mie scattering. With this seeding technique, introduced by Settles and Teng [1982], a bulk liquid solvent is introduced at low flow rates into the boundary layer through a small hole in the wall (static pressure taps are convenient). It issues from the hole as a fog of small droplets formed by the automization of the liquid stream through the shearing action of the surface stress. In this test, acetone and alcohol droplet fogs were imaged using high-speed cinematography with general illumination, and still photography with laser sheet illumination. The laser sheet experiment gave results similar to smoke flow experiments done in low-speed boundary layers, like those of Falco [1977] and Head and Bandyopadhyay [1981]. In the current work, however, single-point rather than spanwise slot injection was used and the boundary layer transition occurred naturally rather than by wire trip.

Since the size of a seed particle determines its ability to follow the flow, an in situ measurement of the acetone and alcohol droplet size distributions was done. A Malvern Instruments Series 2600 laser diffraction particle sizer was employed. The sizing experiment was done in a facility where Re_δ was a factor of two lower than that for the flow visualization experiment. At $y/\delta = 0.5$ in this boundary layer, the mean droplet size for acetone was found to be about 3.2 μm, for ethyl alcohol about 4.5 μm. The difference in size was probably due to the lower viscosity of acetone. A lower viscosity produces smaller droplets due to a higher susceptibility to the shearing process. M. Smith [1989] estimated the frequency response of the droplets to be about 50 kHz. An estimate of the forcing frequency experienced in a large-scale eddy can be made using $f_{eddy} = (U_e - U_c)/\delta$, where U_c is the convection velocity of the eddy (about $0.9U_e$). Since, in the outer layer, the seed only needs to follow the relative velocity between the eddy and the freestream, $U_e - U_c$ is the relevant characteristic velocity. For this flow $f_{eddy} = 2.1$ kHz, leaving a factor of 20 or so in flow following capability to mark fluid motions with a frequency content higher than this fundamental.

4.1
Cine data

Cine droplet data were taken with the same high-speed drum camera used in the cine schlieren experiment. General lighting was provided by a Beckman and Whitley Inc. Model 357 Electronic Flash Unit which provided a constant intensity "flash" lasting several milliseconds, the duration of the complete drum camera film record. Selected sequences of images from the cine droplet experiment are presented in Fig. 5a and 5b. Each figure contains 10 sequential frames, taken at 27 μsec intervals. These images, digitally retouched to remove scratches and correct non-uniform illumination, are reproduced as negatives. The streamwise field of view in each frame is about 3.75δ

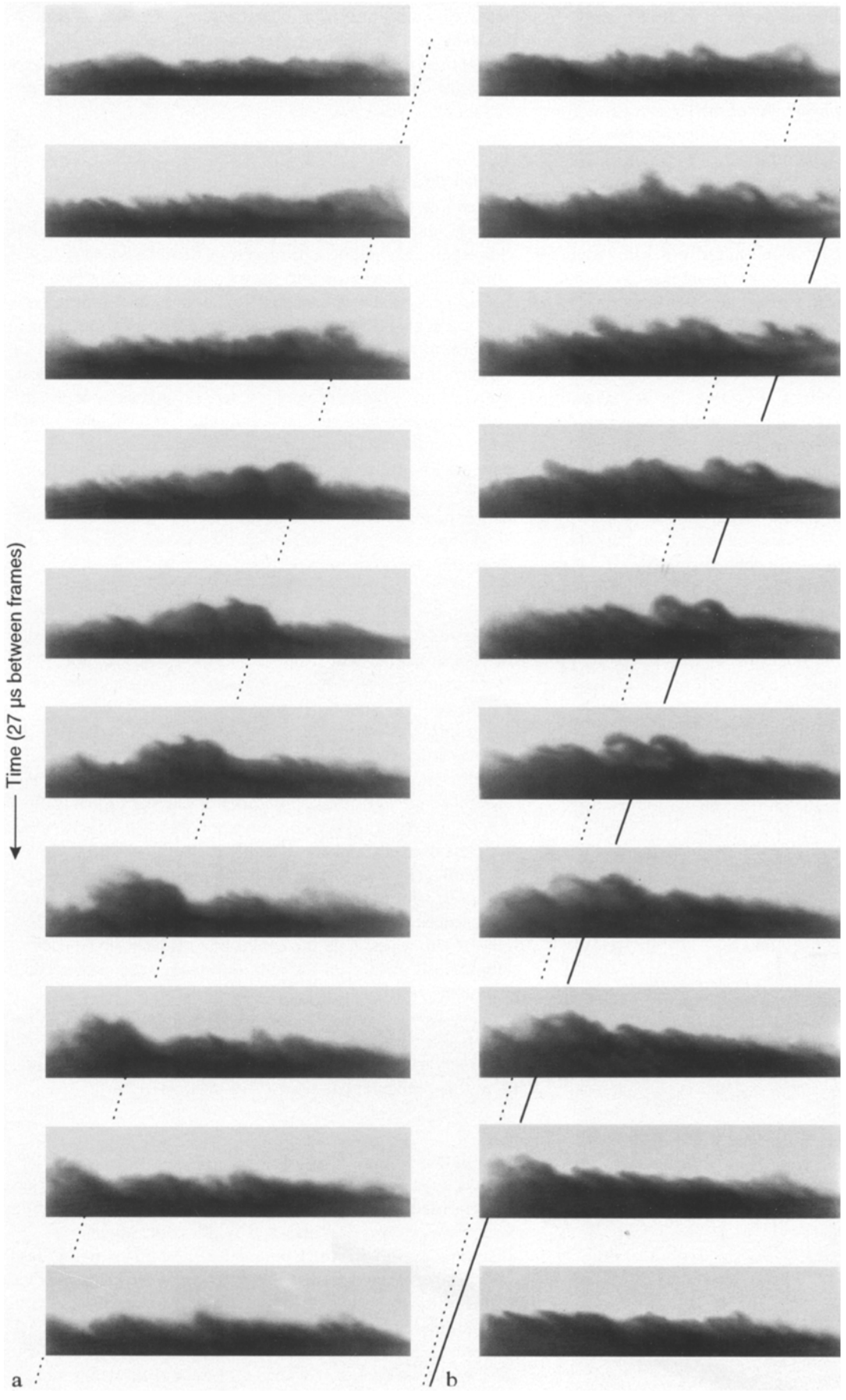

Fig. 5a, b. Cine data in droplet seeded boundary layer. Dashed and solid lines mark velocity trajectories of structures (dashed line, velocity = 0.74 U_e; solid line, velocity = 0.87 U_e)

(about 100 mm). In Fig. 5a and 5b the seed injection point is 8δ upstream of the middle of the field of view.

These specific sequences were selected because they represent two different types of structures which appear throughout the many data records. In Fig. 5a the $x-t$ trajectory of a turbulent bulge lifting from the floor is marked by the dashed line. The slope of the line represents its velocity. In Fig. 5b, a bulge exhibiting roll-up on the scale of δ is marked by a solid line. The dashed $x-t$ trajectory from Fig. 5a is also displayed on Fig. 5b for comparison, to demonstrate that the velocity of the rolled-up bulge (about $0.87U_e$) is greater than the velocity of the bulge that has not rolled-up (about $0.74U_e$).

It is possible that the structures shown here are actually part of a generic structure marked at different stages in its evolution. The instantaneous shear product takes a large value when a clump of low-speed fluid is lifted away from the wall (in this case positive v', negative u'). The clump accelerates downstream and begins to roll up as it interacts with the surrounding turbulent field. If it passes over the injection point early in this process it could appear like the structure shown in Fig. 5a. If it is marked later in its evolution the droplets will be entrained in the structure as it is rolling up and it might look like the feature shown in Fig. 5b.

4.2
Laser sheet data

For the seeded laser sheet experiment, a Kinetic Systems 25W copper-vapor laser running at 30 Hz was used as the light source. Images were acquired at about 1/2 Hz with a Nikon F-1 35 mm camera equipped with a motor drive.

To study the evolution of the large-scale motions, the injection holes were located at several different streamwise positions upstream of the viewing location. Streamwise data sheets taken normal to the wall are given in Figs. 6 and 7. At the bottom of Fig. 6 a scale indicates the streamwise location downstream of the injection hole in units of delta. Delta is defined here as the boundary layer thickness at the center of the field of view. Note the scales in Fig. 7 indicating progressively closer positioning of the injection point to the field of view.

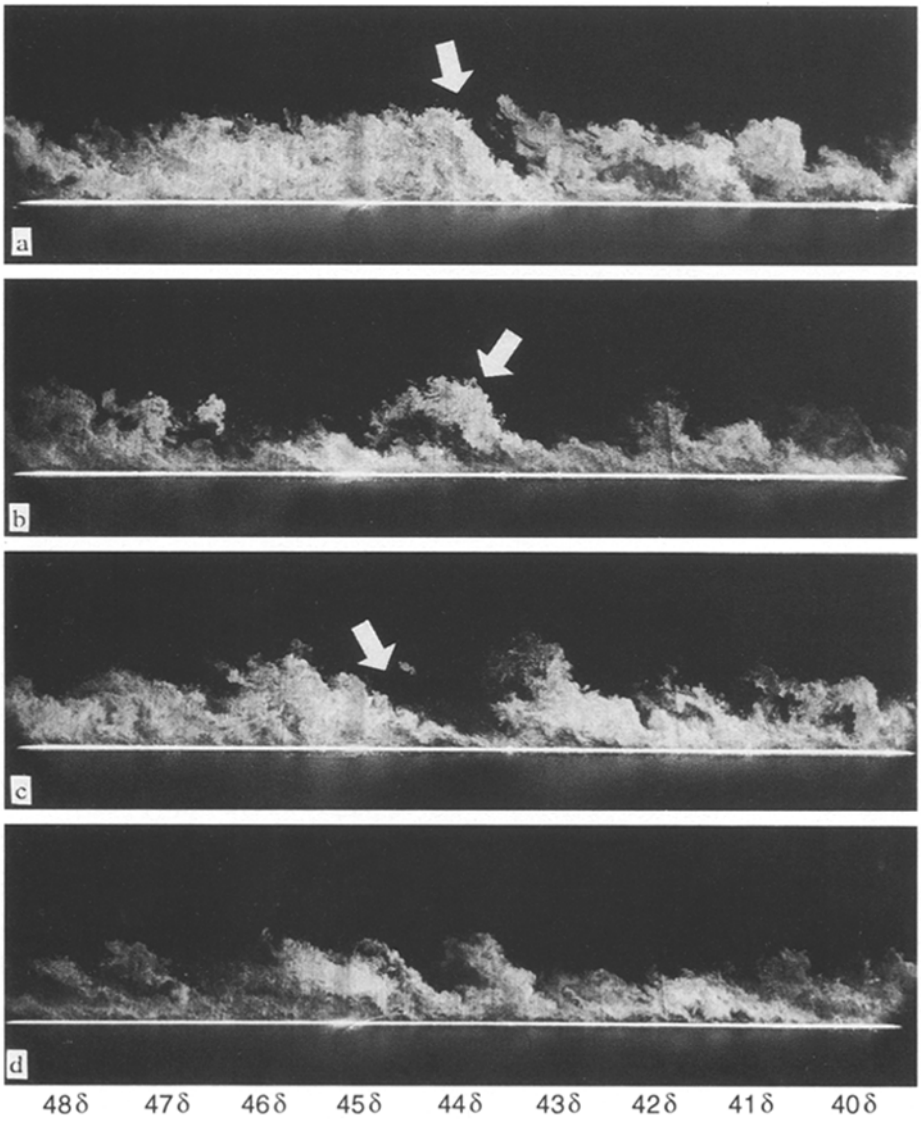

Fig. 6a–d. Pulsed laser sheet data on droplet seeded boundary layer. Arrows mark structures of interest (see Sect. 6). Horizontal axis is marked in units of δ downstream of droplet injection point

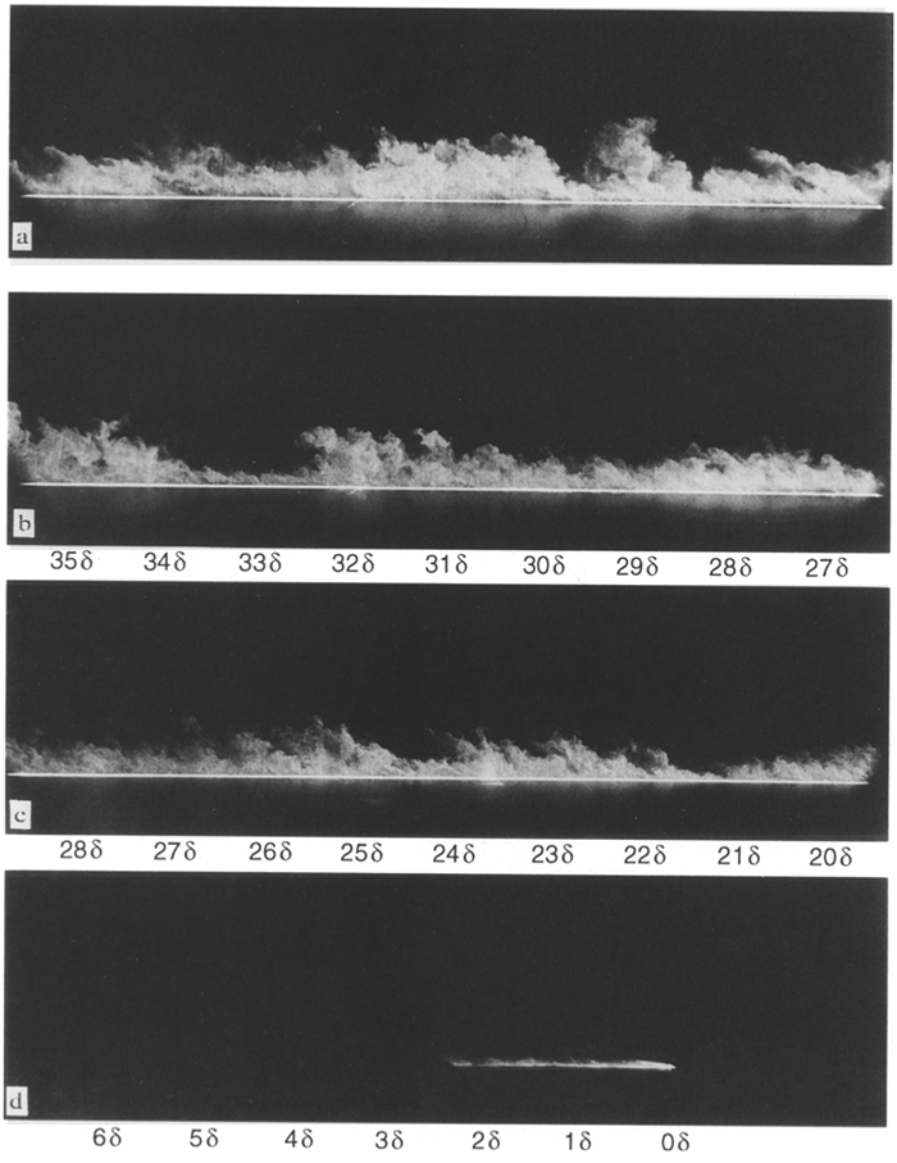

Fig. 7a–d. Pulsed laser sheet data with injection point progressively closer to viewing location

Sheets parallel to the floor were viewed through the top edge of a side window because optical access through the ceiling was not available. These data taken at several heights are given in Fig. 8. Figure 8a has the same injection point and streamwise scaling as Fig. 7b, with $y/\delta = 0.85$. Figure 8b has $y/\delta = 0.5$ and streamwise scale of Fig. 7c. Figure 8c has $y/\delta = 0.25$ and the scale of Fig. 7b. Figure 8d has $y/\delta = 0.25$ and the scale of Fig. 7c.

These particular images were selected to illustrate features representative of those seen in the thousands of data frames taken. The side views show the development of eddies and sets of eddies at various angles to the wall, some with apparent roll-up, others without. The plan views show intermittent strings of eddies, some with regular spacings and, again, some with apparent roll-up and others without.

5
Rayleigh scattering

Below, the results of flow visualizations using Rayleigh scattering are presented. Rayleigh scattering is the scattering of light from particles much smaller than the wavelength of the incident light. It is proportional to the number density of scatterers in a medium. In a gas composed of a single species or in a gas mixture such as air in which the mixture fraction of each component species remains constant, Rayleigh scattering is proportional to the density of the gas. An ultraviolet laser (193 nm) was used to enhance the signal; Rayleigh scattering intensity goes as laser frequency to the fourth power.

Rayleigh scattering has previously been used to examine the structure of incompressible jets. For example, Escoda and Long [1983] used Rayleigh scattering to examine the concentration field of a propane jet, and Yip and Long [1986] used Rayleigh scattering to investigate the structure of a turbulent jet of Freon-12. Miles et al. [1989] used an ArF laser (193 nm) to image a compressible supersonic jet in air. In that case the naturally occurring density fluctuations in the compressible flow of air were observed rather than the mixing of two gasses with different Rayleigh cross sections. This form of the UV Rayleigh scattering technique was applied here to obtain instantaneous

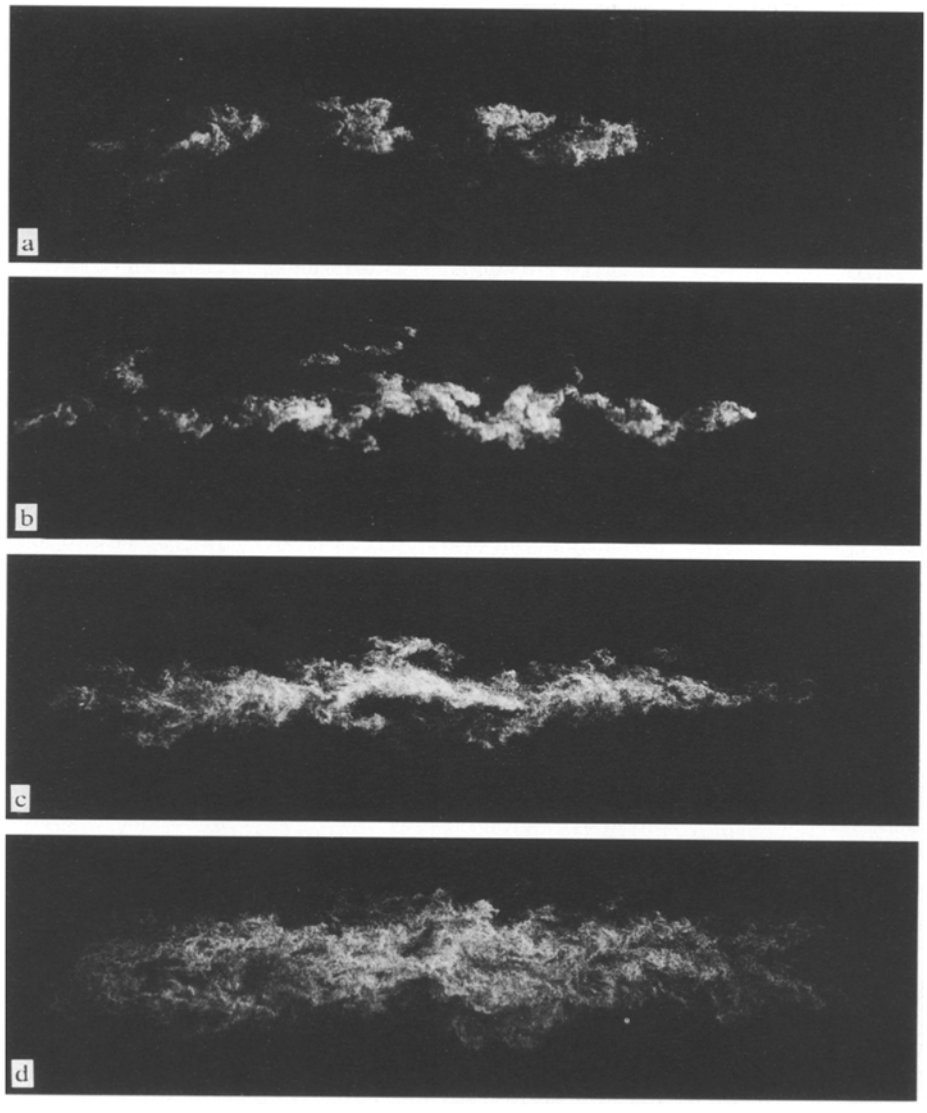

Fig. 8a–d. Pulsed laser sheet data with sheet parallel to the floor at different y/δ locations. See text for heights and horizontal scale

planar images of the Rayleigh scattering cross-section in a Mach 2.5 turbulent boundary layer.

The presence of water in air can have a strong effect on the Rayleigh signal, even for very low water concentrations (parts per million). Upstream of the nozzle, where it is in the gaseous phase, a small water fraction produces a corresponding small contribution to the Rayleigh cross-section. However, as the flow expands through the nozzle, water clusters may be formed by homogeneous nucleation. In this process, a few molecules of water stick together to form a "cluster" (according to Wegener [1969] heterogeneous nucleation is not important in supersonic nozzles where the time-of-flight for a fluid element is very short). Cluster size was measured in moist air by Wegener and Stein [1968] and was found to range from less than 2 nm to about 6 nm, where the diameter increased with increasing moisture content. These extremely small particles, which may consist of agglomerations of as few as 10 molecules, can dominate the Rayleigh signal. In the present case, with a water content of about 14 ppm, the Rayleigh images show the instantaneous number density of these clusters, rather than the air density (see M. Smith [1989] and D. Smith et al. [1991]). The scattering by clusters is still in the Rayleigh regime since the scatterers are much smaller than the wavelength of the incident light.

The boundary layer for this work developed on the wall of a vertical 13 mm × 26 mm wind tunnel. At the imaging location the boundary layer conditions were, $\delta = 4.2$ mm and $Re_\theta = 25{,}000$. One section of the wind tunnel had four quartz walls (Suprasil II) to allow UV optical access. Data were taken in one streamwise plane normal to the boundary and in a series of streamwise planes parallel to the boundary at different y/δ positions. Because the repetition rate of the laser was only 10 Hz, each image was a random sample; the freestream fluid moved about 2000 y/δ between laser pulses.

The rectangular laser beam was shaped using a single cylindrical quartz lens ($f = 200$ mm) to make a uniform sheet about 40 mm × 100 μm. Mean laser energy at the test section was about 25 mJ/pulse delivered in a pulse width of about 10 nsec. Since the power density at the focal plane of the sheet was above the damage threshold of the quartz windows, care had to be taken to keep the focal plane of the sheet away from the window. Therefore the sheet was thinnest about one δ away from the quartz surface, at the outer edge of the boundary layer.

Images were acquired with a General Electric Model TN2505 CID camera fitted with a gated double-microchannel plate intensifier (ITT model F4561) providing an available optical gain of nearly 2 million. A Nikon 105 mm quartz lens, f number 4.5, was used at about 1 : 1 magnification. The image data were stored on 1/2″ video tape for subsequent digital processing.

Figure 9 shows five different streamwise Rayleigh cross-sections normal to the wall. In Fig. 10, a series of sheets taken parallel to the wall is presented. Pairs of independent samples are shown for each y/δ location. Standard image processing techniques were employed on these images to correct for scattering from windows, non-uniform illumination, and detector gain variation (see M. Smith [1989] for processing details).

To interpret these images, the connection between the ice cluster density and the air density must be considered. In the regions where the temperature is below a lower critical value, all the water will be in the form of clusters, and, since the clusters will be uniformly distributed, the cluster density in these regions should be proportional to the air density. In regions where the temperature is above an upper critical value, all the water will be in the form of vapor. Since the Rayleigh cross-section of air (including a small water vapor fraction) is much smaller than that of the clusters, these regions will appear dark when compared to the regions where clusters are plentiful, and no useful information regarding the air density can be obtained. This behavior was demonstrated by D. Smith et al. [1991] by obtaining Rayleigh images of flows passing through shocks. In air with a water content of 14 ppm, when the shock was strong enough, the shock was seen as a line separating upstream bright zones (low temperature) from downstream dark zones (high temperature). In nitrogen, with virtually no water content, the image intensity increased greatly across the shock, accurately reflecting the increase in density. However, since the Rayleigh cross-section of nitrogen is much smaller than that for water clusters in air, D. Smith et al. had difficulty obtaining high signal-to-noise images.

An additional issue for cluster image interpretation is the temporal lag in cluster formation or disintegration. The response of the clusters to a change in temperature and pressure is a non-equilibrium process. There is a relaxation or recovery time required for the disintegration to take place. M. Smith. [1989] studied the shock wave boundary layer interaction generated by a 16° compression corner (under the same operating conditions pertaining to the present boundary layer study) and concluded that in that case the time was quite short, approximately 2 μs.

To study the connection between the air density and the observed Rayleigh signal more closely, the statistics of the Rayleigh signal were examined. A plot of average greyvalue as a function of y/δ is shown in Fig. 11. It was derived from 256-frame averages constructed from ensembles of Rayleigh images taken parallel to the wall. Note that this plot (solid squares) is nearly linear in the outer part of the layer, in agreement with the profile derived from conventional probe surveys (the dashed line). However, near the wall the greyvalues being to increase rather than continuing to decrease as they

Fig. 9. Samples of Rayleigh scattering data taken with an ultraviolet pulsed laser. Sheets streamwise and normal to the boundary

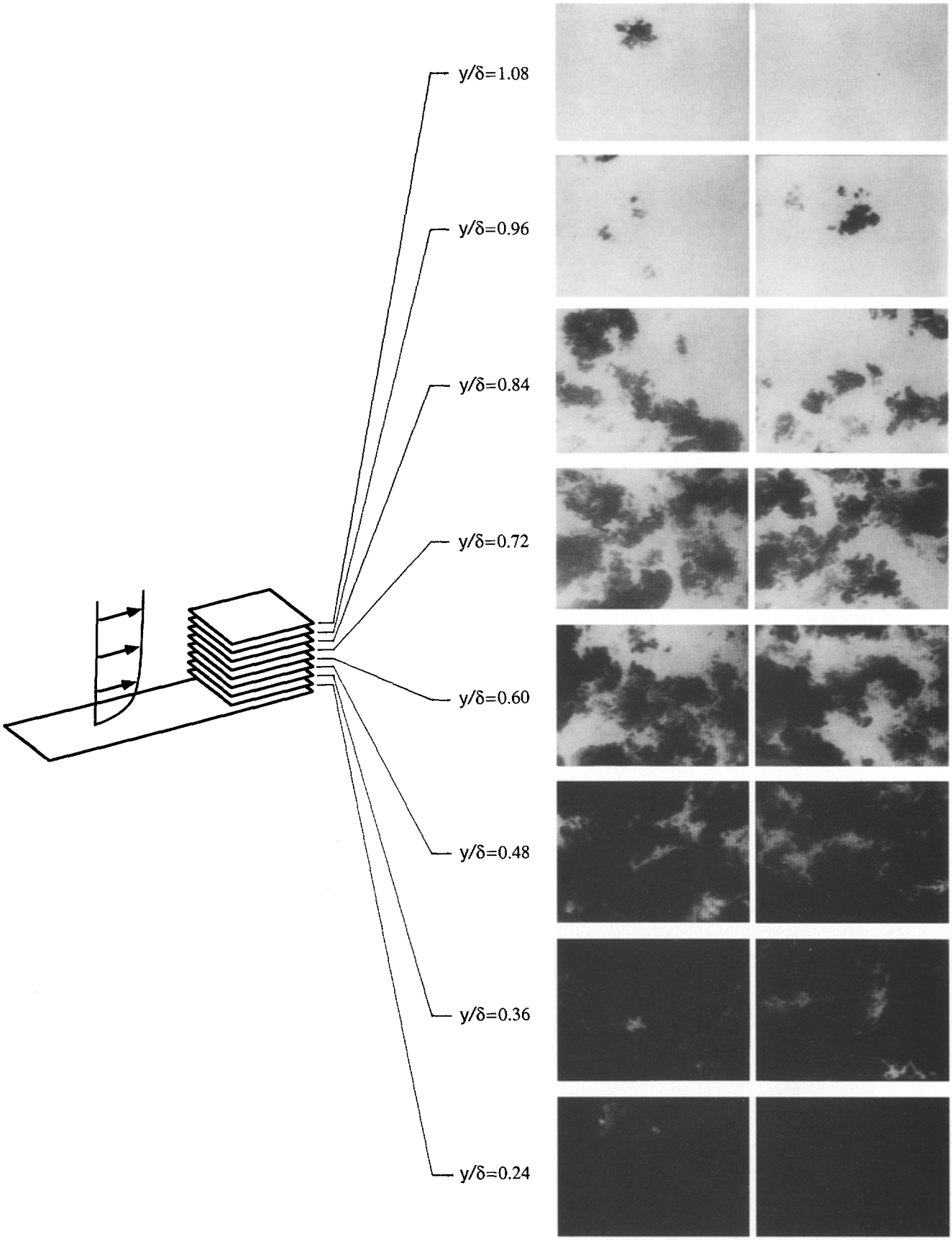

Fig. 10. Rayleigh scattering sheets taken parallel to the wall at decreasing y/δ locations

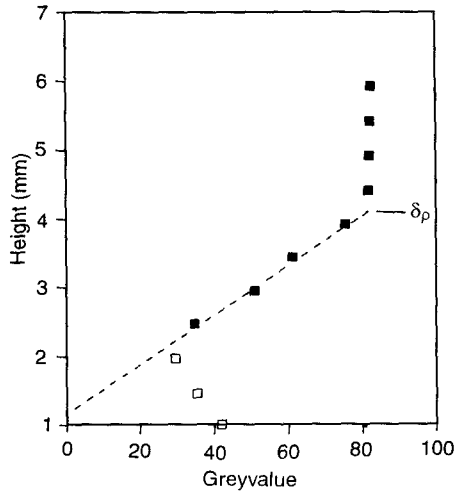

Fig. 11. Averaged Rayleigh signal level as a function of y/δ

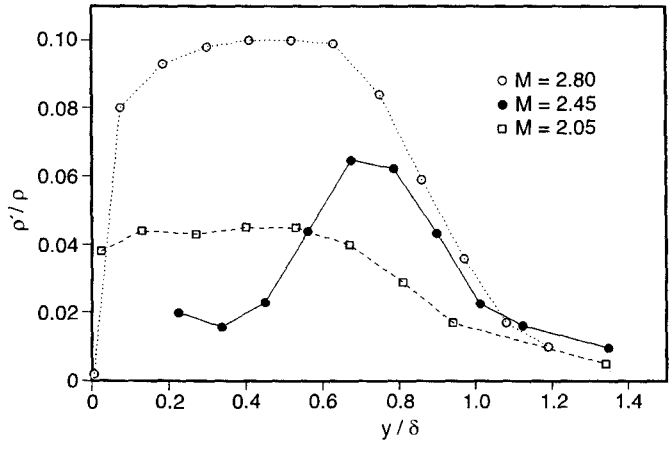

Fig. 12. Normalized rms Rayleigh signal levels compared to hot-wire mass-flux rms values over the width of the boundary layer

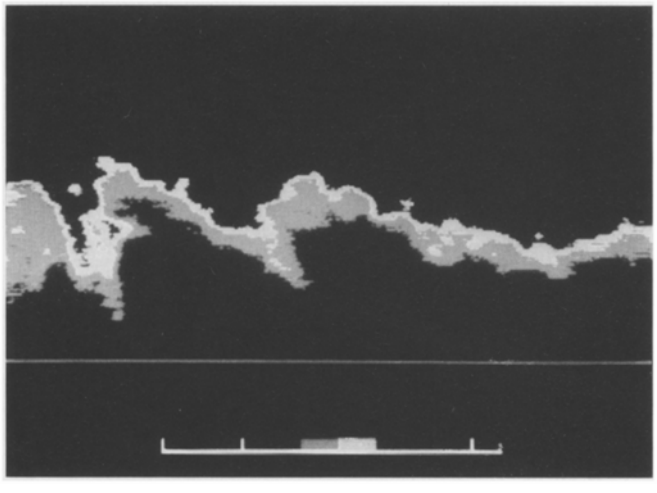

Fig. 13. Rayleigh scattering data color-mapped to illustrate features of the rotational/non-rotational fluid interface (see Sect. 5)

should (these aberrant data are marked by open squares). This was due to light scattered from the window. The images of the lower part of the boundary layer in fig. 10 were shifted by subtracting a constant bias so that their average greyvalues fell on the expected linear mean profile.

As noted earlier, if these images represented the Rayleigh scattering from pure air then dark regions would correspond to regions of low air density. In a compressible boundary layer, frictional heating produces a low density region near the wall. Hence, the images show the expected trend of decreasing mean greyvalue (black = greyvalue 0) with decreasing y/δ. In fact, the mean profile retains the linear shape of the actual density profile over the bulk of the outer layer, even though the Rayleigh data

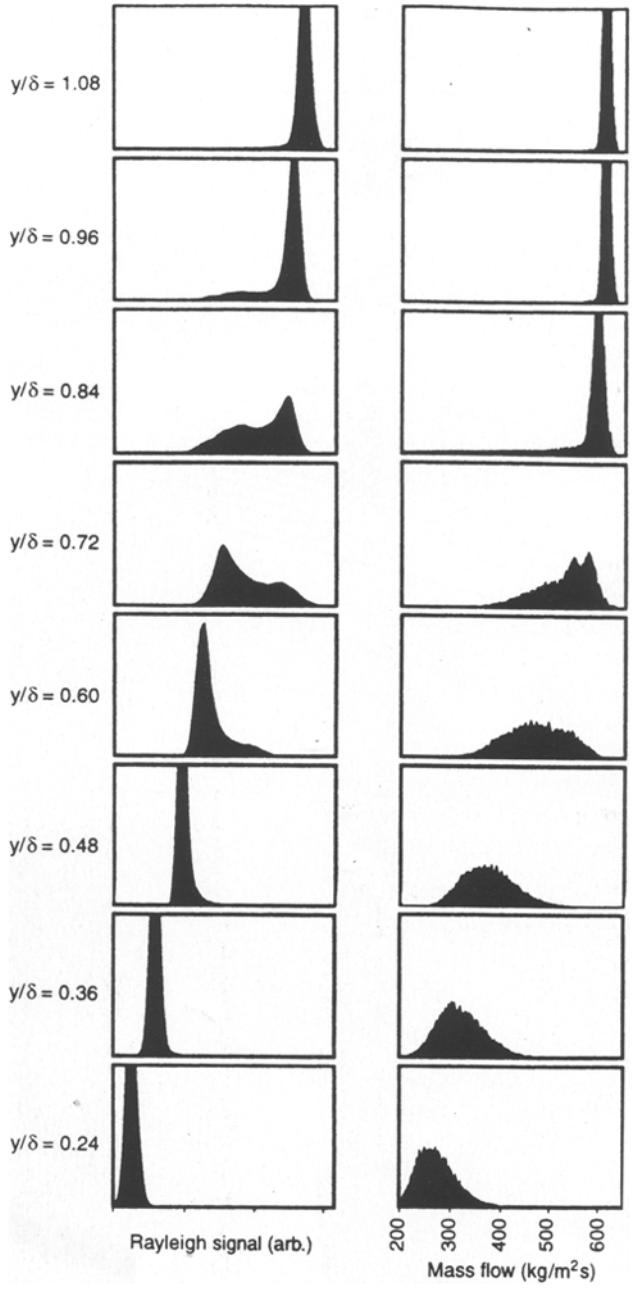

Fig. 14. Comparison of Rayleigh signal pdf's and mass-flux pdf's taken with hot-wires

are thresholded by the disintegration of the clusters which generate the signal.

In Fig. 12 the current normalized rms greyvalues (M = 2.45 case) are compared to previous measurements of the rms density fluctuations in similar boundary layers. It appears that the Rayleigh signal gives a reasonable estimate for the rms level for the outer part of the layer ($y/\delta > 0.65$), but closer to the wall the Rayleigh signal drops off sharply as the clusters break up in this region of higher temperature.

The Rayleigh images are dominated by the sharp interface between the freestream, cluster-marked air and the warmer rotational fluid in which the clusters have presumably disintegrated. Although sharp, the interface is not symmetric around the mean greyvalue. Figure 13 has been color-mapped to accentuate this asymmetry. Note the color map at the bottom of the image. An equal range of pixel values has been mapped to blue above a midrange value, to red below. The relatively smaller layer of red on the outer side of the interface compared to the large layer of blue on the inner side of the interface shows that, moving in from the freestream, the greyvalue across the interface rises quickly at first, then more slowly. This intensity function vs. distance across the instantaneous interface is either due to the disintegration of the clusters with the gradual increase in temperature or with the gradual decrease in density (and the corresponding decrease in cluster number density). In either case, this feature is related, albeit probably non-linearly, to the instantaneous temperature/density field.

In Fig. 14, probability density distributions (pdf's) of greyvalue measured in the Mach 2.5 boundary layer (left) are compared with pdf's of the instantaneous mass-flux measured by Donovan [1989] in the Mach 2.8 boundary layer (right). Knowing that the Rayleigh images are dominated by the sharp interface between cluster-bearing and non-cluster-bearing fluid, the features of the Rayleigh pdf's (21 left) are readily explained. At $y/\delta < 0.5$, the distributions are narrow since the clusters have disintegrated. At $y/\delta > 0.9$, the pdf's are narrow since the freestream fluid is all marked by clusters. At the intermediate levels around $y/\delta = 0.8$, the pdf's are strongly bimodal since here the flow is dominated by inner and outer fluid separated by a sharp interface. Note that the mass-flux pdf's are also bimodal near this height. This suggests that the "inner-fluid/sharp-interface/outer-fluid" structure of the instantaneous large scale features is not an artifact of the cluster disintegration problem in the Rayleigh data.

At lower y/δ the mass-flux pdf's remain relatively broad compared to the Rayleigh pdf's. This clearly is an artifact of the cluster disintegration problem. Another discrepancy between the Rayleigh and mass-flux pdf's is in the apparent height of the boundary layer. The Rayleigh pdf's remain broad to a larger y/δ. This is most likely due to an error in the estimate of δ in the Rayleigh data rather than an actual difference in the character of the measured quantities.

To study the use of Rayleigh scattering as a means of quantifying the "mean structure shape", space correlations were derived from the Rayleigh images. Full-frame two-dimensional space correlations were calculated for both the horizontal and vertical sheets according to,

$$C_{(i,j)} = \frac{\sum_{k=1}^{n} (X_{(i,j)_k} - \bar{X}_{(i,j)})(X_{(\mathrm{ref})_k} - \bar{X}_{\mathrm{ref}})}{\sqrt{\sum_{k=1}^{n} (X_{(i,j)_k} - \bar{X}_{(i,j)})^2} \sqrt{\sum_{k=1}^{n} (X_{(\mathrm{ref})_k} - \bar{X}_{\mathrm{ref}})^2}} \qquad (2)$$

where, C, is the value of the correlation for a given pixel, X is greyvalue, i and j are the row and column indices for the pixel array, ref indicates a value at the correlation reference point (reference pixel), and n is the number of frames used to create the correlation.

Two-dimensional Rayleigh signal correlations were derived from 233 frame ensembles of streamwise sheets normal to the boundary. Figure 15 shows examples taken with reference points at $y/\delta = 0.38$ and $y/\delta = 0.76$. On these images, the brighter the region, the higher the correlation value. Also, black contour levels have been added to the maps at labeled intervals. The countours are elongated and the major axes are inclined to the boundary at angles between 30° and 60°. Hence, the "mean Rayleigh structures" are elongated and face downstream at an angle of between 30° and 60°, depending on the size of the

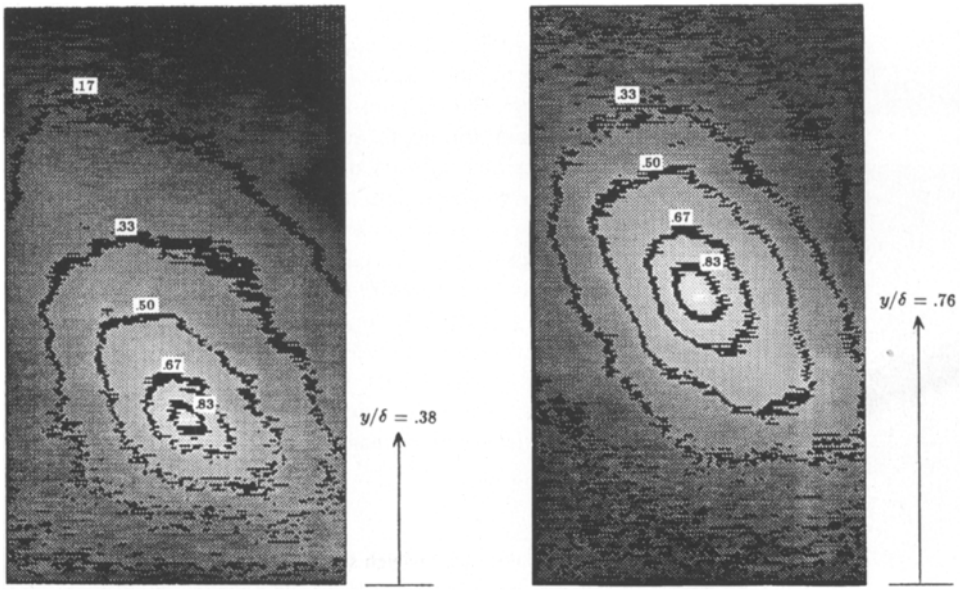

Fig. 15. Two dimensional Rayleigh signal correlation maps taken from 233 frame ensembles of streamwise sheets normal to the wall

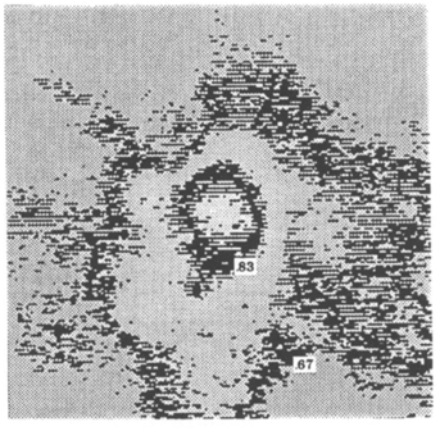

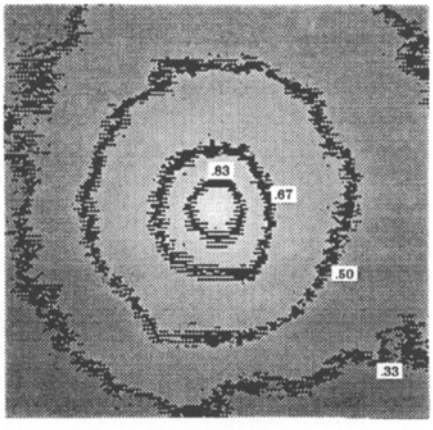

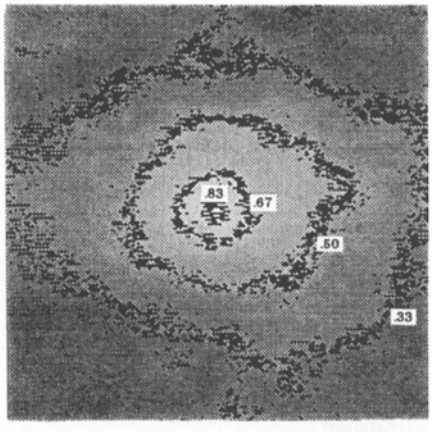

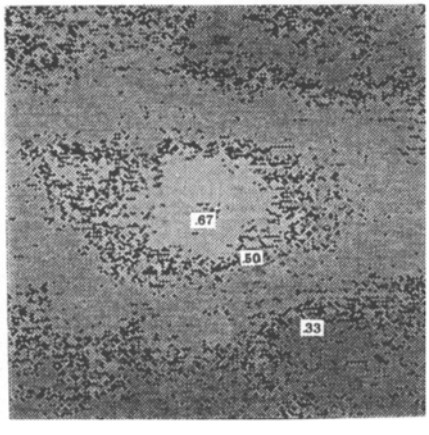

Fig. 16. Correlation maps at different y/δ locations taken from ensembles of Rayleigh sheets parallel to the wall

Fig. 17. Rayleigh sheet taken parallel to the wall, color-mapped to resemble turbulent bulge in the atmospheric boundary layer

feature. This observation is in good agreement with the space-time correlation contours based on mass flux obtained by Spina et al. [1989] in the Mach 2.8 flow using hot wires. Hence, despite the difficulties in interpreting these Rayleigh images, they are useful for establishing spatial correlations.

Correlation maps for density cross-sections taken parallel to the boundary are presented in Fig. 16. These represent ensembles of about 240 frames at each location. Note that the shape of the contours changes over the height of the boundary layer. In the outer part the contours are nearly circular, but nearer the wall there is some elongation in the streamwise direction. These observations are again in good agreement with the space-time correlation contours obtained by Spina et al. [1989] using hot-wire anemometry.

Although spatial correlations provide a concrete way of making quantitative comparisons, the Rayleigh data can be used to make fascinating, though less conventional comparisons. In Fig. 17, a Rayleigh sheet taken parallel to the wall has been color mapped to appear like the base of a cumulus cloud deck. The resemblance is not accidental, and demonstrates that turbulent bulges in the high Reynolds number atmospheric turbulent boundary layer (i.e. cumulus clouds), share qualitative features with those in the high Reynolds number supersonic turbulent boundary layer. Clouds (and other natural features like mountain peaks and ocean waves) are sometimes generated in the motion picture industry using multi-fractals. A comparison of the current Rayleigh data to such naturally occurring fractal features suggests, as others have argued (e.g. Sreenivasan and Meneveau [1986]), that fractal mathematics may be relevant to the description of laboratory turbulent fluid flows. Sreenivasan and Johnson [1989], then Poggie [1990], respectively estimated the fractal dimension of the Rayleigh image interfaces in the Mach 2.5 and Mach 2.8 data. Both studies found that the dimension was lower than corresponding values derived from smoke flow visualization images obtained in subsonic boundary

layers. This supports, in a quantitative way, the observation by Owen et al. [1975] that the boundary layer in a supersonic flow is less intermittent than in a subsonic flow.

6
Discussion and conclusions

The flow visualization techniques presented here provide a number of ways of looking at the structure of supersonic turbulent boundary layers.

In the schlieren experiments, the dominant feature was found to be a positive density-gradient structure, which appears as a finger-like density discontinuity apparently attached to the wall and inclined at an angle of about 45°. It was suggested that positive and negative density gradient features defined the upstream and downstream boundaries of low density fluid bulges. In the Rayleigh experiment, these bulges were visible in planar cross sections. The presence of water clusters made the quantitative interpretation of the images difficult, but in the outer part of the layer the Rayleigh signal images appeared to follow the instantaneous temperature (or density) field reasonably well. The results suggest that in the outer region the temperature (and density, and velocity) varies little within a turbulent bulge, and that a simplistic model for the outer layer might consist of an array of regularly spaced uniform low-density bulges separated from a uniform higher density freestream by a sharp, instantaneously ragged interface.

From the cine schlieren experiment the average velocity of the bulges was determined to be approximately $0.9U_e$. However, with this path-integrated optical technique it was difficult to say much about the evolution of the structures. The cine droplet seeding experiment provide the most information in this regard. It demonstrated that δ-sized bulges could be born explosively, erupting violently from the floor. It also demonstrated the process of roll-up and related it to the passage of "weaker", faster-moving structures. These structures appeared weaker in the sense that they were less able to resist the freestream momentum and thus travelled closer to the freestream velocity. If the explosive, slower, violent structures and the weaker, faster structures were actually just the same generic structure marked at different stages of development, then roll-up is a sign of a mature bulge. That is, the generic turbulent bulge rolls up late in its evolution, after it has reached a stable convection velocity of about $0.9U_e$, and perhaps, after the most violent shear-stress-producing activity has concluded.

The instantaneous planar stills of the acetone-droplet-seeded boundary layer were the most detailed images acquired. They showed strong interfaces between marked and unmarked fluid (e.g. Fig. 6, top arrow), regions of large-scale roll-up, (e.g. Fig. 6, middle arrow) and the formation of intermediate size eddies into δ-sized interfaces (e.g. Fig. 6, bottom arrow)

These data, taken together with the collection of hot-wire data, suggest the diagram of the structure of an outer layer bulge presented in Fig. 18. Such a bulge can support Reynolds shear stress in three ways:

1. By its birth. A packet of fluid with less than average u and positive v contributes to the mean Reynolds stress. The bulge born in Fig. 5a is such a packet.

2. By its stable convection at about $0.9U_e$ with a component of vorticity parallel to the floor. With this vorticity component it acts as a pump drawing high momentum fluid down into the layer. Using hot wires, Spina et al. [1991] found Reynolds stress along bulge interfaces. It may have been of this type.

3. By sustaining smaller scale eddies along its borders or within its interior. It is likely, for instance, that the sub-δ-scale eddies along the interface in the planar droplet data (Fig. 6, bottom arrow) play a role in sustaining the Reynolds stress.

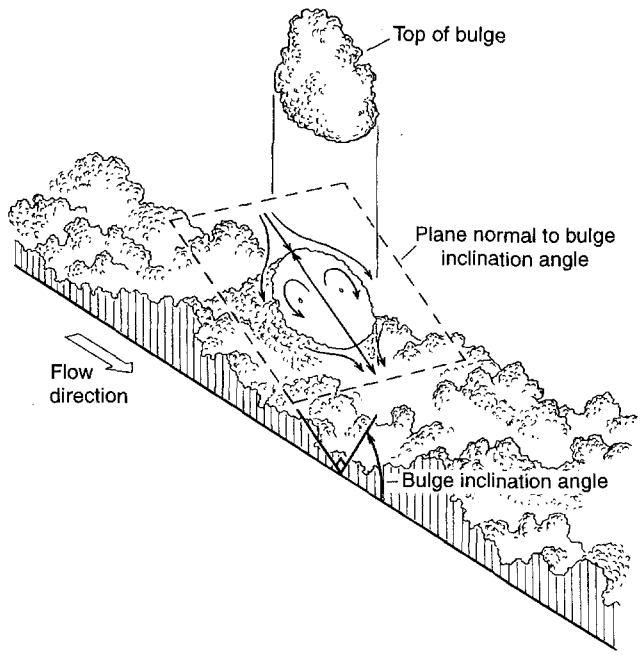

Fig. 18. Suggested structure of a turbulent bulge in a supersonic boundary layer

References

Blackwelder R; Kaplan RE (1976) On the wall structure of the turbulent boundary layer. J Fluid Mech 76: 89

Cogne S; Forkey J; Miles RB; Smits AI (1993) The evolution of large-scale structures in a supersonic turbulent boundary layer. To appear Proceedings Symposium on Transitional and Turbulent Compressible Flows, ASME Fluids Engineering Conference, Washington, D.C., June 20–24

Deckker BEL (1982) Boundary layer on a shock tube wall and at a leading edge using schlieren. In: Flow visualization II, ed. W. Merzkirch, pp. 413–417, Washington: Hemisphere

Donovan JF (1989) The structure of supersonic turbulent boundary layers subjected to concave surface curvature. Ph. D. Thesis, Princeton Univ., Princeton, N. J.

Escoda MC; Long MB (1983) Rayleigh scattering measurements of the gas concentration field in turbulent jets. AIAA J 21: 81

Falco RE (1977) Coherent motions in the outer region of turbulent boundary layers. Phys Fluids 20: 124

Fernholz H; Finley PJ (1980) A critical commentary on mean flow data for two dimensional compressible turbulent boundary layers. AGARDograph no. 253

Head MR; Bandyopadhyay P (1981) New aspects of turbulent boundary layer structure. J Fluid Mech 155: 441

Miles RB; Conners J; Markovitz E; Howard P; Roth G (1989) Instantaneous supersonic velocity profiles in an underexpanded jet by oxygen flow tagging phys Fluids A 1: 389

Morkovin MV (1962) Effects of compressibility on turbulent flows. Int. Symp. on The Mechanics of Turbulence, 367. C.N.R.S., Paris

Owen FK; Horstman CC (1972) On the structure of hypersonic turbulent boundary layers. J Fluid Mech 53: 611–636

Owen FK; Horstman CC; Kussoy MI (1975) Mean and fluctuating flow measurements of a fully-developed, non-adiabatic hypersonic boundary layer. J Fluid Mech 70: 393

Poggie J (1990) MS Thesis, Dept. Mech. Aerosp. Engin., Princeton University

Settles GS; Teng HY (1982) Flow visualization of separated 3-D shock wave/turbulent boundary layer interactions. AIAA Paper 82-0229

Smith DR; Poggie J; Konrad W; Smits AJ (1991) Visualization of the structure of shock wave turbulent boundary layer interactions using Rayleigh scattering. AIAA Paper 91–0651,

Smith DR; Smits AJ (1993) Simultaneous measurement of velocity and temperature fluctuations in the boundary layer of a supersonic flow. Experimental Thermal and Fluid Science 7: 221–229

Smith MW (1988) Cinematic visualization of coherent density strucutures in a supersonic turbulent boundary layer. AIAA Paper 88-0500

Smith MW (1989) Flow visualization in supersonic turbulent boundary layers. Ph. D. Thesis, Princeton Univ., Princeton, NJ

Spina EF; Smits AJ (1987) Organized structure in a compressible turbulent boundary layer. J Fluid Mech 182: 85–109

Spina EF; Donovan JF; Smits AJ (1991) On the structure of high-reynolds-number supersonic turbulent boundary layers. J Fluid Mech 222: 293–327

Sreenivasan KR; Johnson A (1989) Private communication

Sreenivasan KR; Meneveau C (1986) The fractal facets of turbulence. J Fluid Mech 173: 357–386

Van Dyke M (1982) An album of fluid motion. The Parabolic Press, Stanford, CA

Wegener PP (1969) Gasdynamics, A Series of Monographs Vol. 1, Nonequilibrium Flows, Part 1. Marcel Dekker, New York and London

Wegener PP; Stein GD (1968) Light-scattering experiments and theory of homogeneous nucleaton in condensing supersonic flow. proc. Twelfth International Symposium on Combustion, Poitiers, France

Yip B; Long MB (1986) Instantaneous planar measurements of the complete three dimensional scalar gradient in a turbulent jet. Optics Letters 11: 64–66